FERMILAB-PUB-20-564-TD
(accepted)
Journal of Alloys and Compounds

The strong influence of Ti, Zr, Hf solutes and their oxidation on microstructure and performance of Nb_3Sn superconductors

X. Xu [a, *], X. Peng [b], J. Rochester [c], M.D. Sumption [c], J. Lee [a], G.A. Calderon Ortiz [c], J. Hwang [c]

[a] *Fermi National Accelerator Laboratory, Batavia, IL 60510, USA*

[b] *Hyper Tech Research Incorporated, 539 Industrial Mile Road, Columbus, OH 43228, USA*

[c] *Department of Materials Science and Engineering, the Ohio State University, Columbus, OH 43210, USA*

* Corresponding author. *E-mail address: xxu@fnal.gov*

Abstract

Over the last few years a new type of Nb_3Sn superconducting composite based on the internal oxidation approach has emerged and has demonstrated performance significantly superior to conventional Nb_3Sn. It requires a supply of O and the use of a Nb alloy – Nb-X, where X is a solute element that can be selectively oxidized to form oxide particles within the Nb_3Sn. Such oxide particles not only refine Nb_3Sn grain size, but also have the proper size to act as artificial pinning centers (APC) directly restraining fluxon motion, and thus dramatically improve superconducting properties. In this article we show that the size and volume fraction of the oxide particles determine both the levels of grain refinement and the shift in the peak field of the flux pinning force (F_p-B) curve. We explore the factors influencing these microstructure and properties, which we find include: selection of the solute element X, solute content, O content, and heat treatment. For the selection of X, we searched the periodic table for all promising candidates but focused down on the group-IVB elements (Ti, Zr, Hf) here as the drawability of Nb_3Sn wires made from Nb-Ti, Nb-Zr, and Nb-Hf alloys has been demonstrated in the past few decades. We found that while internally oxidizing Nb-1.5at.%Ti led to negligible grain refinement and F_p-B peak shift, Nb-Zr alloys led to much more dramatic results, and internally oxidizing Nb-Hf alloys led to the strongest grain refinement and F_p-B peak shift. For Hf alloying in particular, we compared our internal oxidation method with another method for grain refinement, which uses Hf alloying itself without oxidation, and found that internal oxidation led to much stronger grain refinement and F_p-B peak shift. We also found that higher solute content and lower reaction temperature led to stronger grain refinement and F_p-B peak shift. We conclude with a discussion of the possible mechanisms for the influence of these factors.

Keywords: Nb_3Sn superconductor, Internal oxidation, Grain size, Precipitation, Flux pinning

1. Introduction

Nb_3Sn superconductors have important applications in the building of high-field magnets. Research and development of Nb_3Sn conductors is regaining significant interest worldwide, for

two main reasons. First, the proposed Future Circular Collider (FCC) plans to use Nb_3Sn conductors to produce its dipole and quadrupole magnets [1]; however, the FCC-required performance, particularly the critical current density (J_c), is significantly higher than what state-of-the-art Nb_3Sn can deliver [2,3], motivating efforts to further improve this technical superconductor. Second, although the J_c level of the state-of-the-art Nb_3Sn has been more or less at a plateau for nearly two decades [4], some recent research and development has demonstrated that Nb_3Sn still have significant room for further improvement. One such advance was our successful application of the internal oxidation method to Nb_3Sn wires [5,6], which has led to a new type of Nb_3Sn with performance significantly superior to that of conventional Nb_3Sn [5]. This has inspired a few groups to research into this promising approach [7-10]. Another development fostering progress was that recently the Florida State University (FSU) group, when in a follow-on study of the internal-oxidation Nb_3Sn for Ta doping, discovered that Hf alloying itself could refine Nb_3Sn grain size even without internal oxidation, and thus proposed to use the non-oxidation Hf-alloying approach to improve Nb_3Sn J_c [11]. In fact, it is interesting that Tachikawa et al., who heavily studied Nb_3Sn wires with doping of group-IVB elements (Ti, Zr, Hf) in the 1980s (e.g., [12,13]), reported that addition of Ti, Zr, or Hf to Nb led to appreciably finer Nb_3Sn grain size for the reaction temperature of 800°C, but not much for 700°C [12]. The FSU group further showed that Hf alloying could still refine Nb_3Sn grain size for low reaction temperatures (650-675°C) and clarified its mechanism in terms of suppression of Nb recrystallization [11].

In general, a subelement of a conventional Nb_3Sn wire before heat treatment is composed of precursors including a Sn-source core (e.g., Sn+Cu) in a Nb alloy tube or variant (e.g., an annulus composed of Cu-clad Nb rods for rod-restack-process, RRP®, wires). Ti or Ta doping (e.g., via Nb-4at.%Ta alloy) is used to improve Nb_3Sn upper critical field [14]. In contrast, fabrication of an internal-oxidation-type Nb_3Sn subelement requires two modifications: (1) the Nb or Nb-4at.%Ta must be replaced by a suitable Nb-X or Nb-4at.%Ta-X alloy for internal oxidation (where X is a solute element in Nb), (2) a proper oxide must be added into the subelement, which must have a design that allows oxygen transfer to the Nb alloy [15]. In the early stages of heat treatment O diffuses to the Nb alloy and dissolves in it; subsequently, while the Nb_3Sn layer grows, the X solute is selectively oxidized to form oxide nanoparticles in the Nb_3Sn matrix. These particles can significantly refine Nb_3Sn grain size (by a factor of two or greater [15]). This method significantly improves Nb_3Sn J_c: e.g., the internal-oxidation-type wires we developed recently using a Nb-4at.%Ta-1at.%Zr alloy, with either 61 or 217 filaments, have achieved the FCC non-Cu J_c specification [16,17]. In fact, the layer J_c of the internally-oxidized Nb_3Sn is 2-3 times of that of the state-of-the-art RRP® conductors at 16-20 T [18].

A proper understanding of the mechanism by which internal oxidation improves J_c is important for further development of Nb_3Sn conductors. The J_c of a superconductor at a given B is determined by the total available flux pinning force per unit volume, F_p, as $J_c = F_p/B$. Because grain boundaries were known to be the primary flux pinning centers for conventional Nb_3Sn conductors [19] and the maximum pinning force ($F_{p,max}$) increases dramatically as the grain size decreases [20,21], the J_c improvement in internally-oxidized Nb_3Sn was, early on, interpreted primarily in terms of its refined grain size. However, our recent work, which designed an experiment to compare two conductors with similar average grain size (~85 nm), one with oxide

precipitates and the other without, showed that the one with precipitates had significantly higher flux pinning and J_c [16]. This is because the oxide precipitates, most of which have a particle size below 10 nm, serve as "artificial pinning centers" (APC), which directly pin fluxons and make a significant contribution to the total F_p due to their high volumetric density [16]. An evidence supporting this is the change of the F_p-B curve shape for internally-oxidized Nb_3Sn. All conventional Nb_3Sn wires produced over the past five decades generally follow Kramer's law with F_p-B curves peaking at ~0.2B_{irr} (B_{irr} is the irreversibility field – the field at which J_c vanishes), known to be a characteristic of "surface pinning" [22]. In contrast, the F_p-B peak of internally-oxidized APC Nb_3Sn is found to shift to higher fields [5,15,16]. This is believed to be due to the addition of the precipitates-contributed "point pinning", for which the F_p-B curves peak at 1/3 of B_{irr} [23]. The shift of F_p-B peak to higher fields leads to a flatter J_c-B curve, which enhances J_c at high fields (e.g., above 10 T) but reduces J_c at low fields (e.g., below 3 T). Apart from the increase in $F_{p,max}$ due to grain size reduction and addition of point pinning, as well as the shift of $F_{p,max}$ to higher fields, we also found that internal oxidation can improve Nb_3Sn B_{irr} [17], which also contributes to enhancement of high-field J_c. Overall, internal oxidation does not enhance Nb_3Sn J_c via a single mechanism, but by several distinct influences on the microstructure and properties of Nb_3Sn.

In this work we explore factors that influence the microstructure and pinning properties of internal-oxidation Nb_3Sn. We find that one key influencing factor is the alloying element X. We chose Zr for our past work [5,15-18] mainly because of the availability and low cost of the commercial Nb-1%Zr alloy, which is important for large-scale conductor productions. In this work we explore other possible options to see if there is any other element that can lead to more optimized internal oxidation effects. As explained later, we searched the periodic table for all promising candidates and focused down on Ti, Zr, and Hf solutes for this work, as drawability of Nb_3Sn wires made from Nb-Ti, Nb-Zr, Nb-Hf alloys has been demonstrated in the past few decades (e.g., by Tachikawa et al. in the 1980s for Ti, Zr, Hf doping to improve Nb_3Sn B_{irr} [12,13], and later by Hong et al. who used Nb-Hf alloys with high Hf contents to generate Hf precipitates in Nb_3Sn [24], as well as the recent results from the FSU group [11]). Another key influencing factor is oxygen content. The results by Balachandran et al. showing that non-oxidation Hf alloying could also refine Nb_3Sn grain size [11] have led to a hypothesis that the grain refinement in Hf-alloyed Nb_3Sn, whether internally oxidized or not, might be because the grain size of the precursor Nb alloy is smaller (as a result of suppression of Nb recrystallization by Hf). This is an interesting question. In order to clarify the mechanism for grain refinement in internally-oxidized Nb_3Sn, which is important for Nb_3Sn conductor development, here we also compared Hf-alloyed wires with and without internal oxidation. This is a complement to our main focus, which is an exploration of the influence of solute choice, solute content, and heat treatment on the size and distribution of the internal oxidation generated precipitates, and their influence on grain size and pinning properties.

2. Experiments

2.1. Experimental materials

To search for all suitable elements for internal oxidation of Nb_3Sn, we should keep in mind that a suitable solute X must satisfy two prerequisites. First, X must have an affinity to O that is much higher than that Nb does, such that X can be selectively oxidized while the Nb is left non-oxidized and available for Nb_3Sn formation. Second, X must have a considerable solubility in Nb (e.g., a few atomic percent) in order to obtain a Nb-X alloy that has: (1) a solute content large enough to form a dense array of X-oxide precipitates, and (2) good ductility, because the precursor wires must undergo large area reductions without breakage during fabrication. This requirement on solubility in Nb precludes a number of elements, such as the alkaline earth and the rare earth elements, despite their very strong affinity to O. Based on the above prerequisites, we see only a few promising candidates, which include Al and the group-IVB metals (Ti, Zr, Hf). Nb-Al will be explored in a later study, while this work focused on Nb-Ti, Nb-Zr, Nb-Hf alloys, whose suitability for making Nb_3Sn wires has been demonstrated in the past few decades [12,13,24]. Recently Nb-Ti alloy was tried for internal oxidation by Buehler et al., but it was not certain whether the Nb-Ti alloy took sufficient oxygen [10]. For the completeness of this study, we used the standard Nb-4at.%Ta alloy as a reference.

For the exploration of Ti as the solute, we used a Nb-1.5at.%Ti alloy. For Zr, we studied two alloys – Nb-4at.%Ta-0.63at.%Zr and Nb-4at.%Ta-1at.%Zr – in order to see the influence of solute content. Here Ta was used to improve Nb_3Sn B_{irr}. For Hf, we used Nb-4at.%Ta-1at.%Hf. For an initial study, we first fabricated a monofilament for each alloy. As we found that internal oxidation of Nb-1.5at.%Ti did not lead to noticeable grain refinement or F_p-B peak shift, we did not proceed to fabricate multifilamentary wires using Nb-Ti, and thus the monofilament results are reported here. On the other hand, internal oxidation of the Nb-4at.%Ta-1at.%Hf led to significant grain reduction and F_p-B peak field shift, encouraging us to fabricate multifilamentary wires using the Nb-4at.%Ta-1at.%Hf alloy. Tube materials were used for fabrication of all of the wires. Each Nb alloy tube was filled with a mixture of Sn, Cu, and SnO_2 powders (all of these wires had similar Cu/Sn, Nb/Sn, and O/Nb ratios [16]) and then inserted into a pure Cu tube and drawn to a stacking size; 48 such composites and 13 pure Cu rods were stacked into a pure Cu can to constitute a multifilamentary billet (which is called a 48/61 design), and the assembly (with a starting diameter of 19 mm) was drawn to a final wire size of 0.71 mm diameter. In order to compare the effects of the internal-oxidation Hf-alloying approach to the non-oxidation Hf-alloying approach, we also fabricated a wire with the 48/61 design using the same Nb-4at.%Ta-1at.%Hf alloy tube but without any SnO_2 addition. All of the wires were fabricated at Hyper Tech Research Inc. and drew well without breakage; a summary of the wires is shown in Table 1. Among these wires, the one using Nb-4at.%Ta-0.63at.%Zr was described in detail in [18] (with the sample name of "APC-A"), and the one using Nb-4at.%Ta-1at.%Zr was described in detail in [16] (with the sample name of "IO61-2"). In this paper the wires with an internal oxygen source are called out by their Nb alloy compositions, while the wire made with Nb-4at.%Ta-1at.%Hf but without an internal oxygen source is denoted 1Hf-noO.

Table 1. Wire design, chemistry, and reaction heat treatment.

Wire name	4Ta	1.5Ti	0.6Zr	1Zr	1Hf	1Hf-noO

Nb alloy	Nb-4at.%Ta	Nb-1.5at.%Ti	Nb-4at.%Ta-0.63at.%Zr	Nb-4at.%Ta-1at.%Zr	Nb-4at.%Ta-1at.%Hf	Nb-4at.%Ta-1at.%Hf
O amount[a]	Sufficient	Sufficient	Sufficient	Sufficient	Sufficient	No O added
Wire design	48/61	mono	48/61	48/61	48/61	48/61
Diameter, mm	0.71	0.33	0.71	0.71	0.71	0.71
Heat treatment	675°C/90h	675°C/250h, 650°C/350h	675°C/152h	675°C/250h, 700°C/73h	675°C/280h, 700°C/91h	675°C/70h, 650°C/126h

[a]: The O content in each Nb alloy was estimated from its critical temperature by measuring its magnetization versus temperature curve [5,15].

All of the wires were heat treated under vacuum with an initial ramp (at 30°C/h) up to 675°C and held for durations longer than needed for full reactions. The 1Zr and 1Hf wires were also reacted at 700°C so that the influence of reaction temperature could be seen. The 1.5Ti and 1Hf-noO wires were also reacted at 650°C to see if noticeable F_p-B peak shift could be obtained. Scanning electron microscopy (SEM) images of 1.5Ti-650°C/350h, 1Zr-700°C/73h, 1Hf-700°C/91h, 1Hf-noO-650°C/126h are shown in Fig. 1, while SEM image of 0.6Zr-675°C/152h can be found in [18].

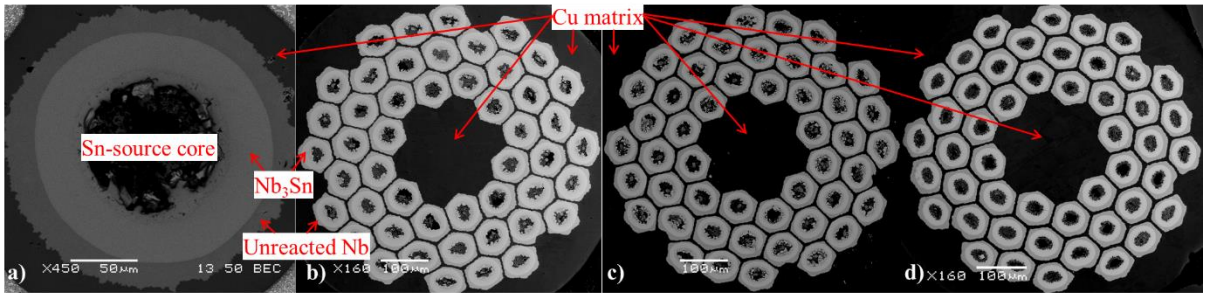

Fig. 1. SEM images of (a) 1.5Ti-650°C/350h, (b) 1Zr-700°C/73h, (c) 1Hf-700°C/91h, and (d) 1Hf-noO-650°C/126h.

2.2. Measurements

Taking advantage of the inter-granular fracture mode of Nb_3Sn, the as-reacted wire samples were fractured and high-resolution SEM images of their cross sections were taken to obtain their grain sizes. To observe the oxide particles, we used both high-resolution SEM and transmission electron microscopy (TEM), as we found that the TiO_2 particles were large enough to be observed via high-resolution SEM in well-polished cross sections, but observation of ZrO_2 or HfO_2 particles, which were mostly below 10 nm, had to rely on TEM.

All of the reacted wires were measured using a Vibrating Sample Magnetometer (VSM) attached to a Physical Property Measurement System (PPMS®). The applied magnetic field was perpendicular to the wire axes, and had a 13 mT/s ramp rate. Magnetic moment versus field (M-B) loops were measured at 4.2 K to calculate the F_p-B curves. The peak field of an F_p-B curve is denoted "B_p" here.

3. Experimental Results

3.1. Oxide particle size

Electron microscopy found no oxide particles in the 4Ta sample. SEM and TEM images displaying TiO_2, ZrO_2 and HfO_2 particles in the 1.5Ti-675°C/250h, 1Zr-700°C/73h, and 1Hf-700°C/91h samples are shown in Fig. 2, respectively. The oxide particle size was observed to vary across the Nb_3Sn layer for all the three samples. In Fig. 2 we show regions close to the outer boundaries of the Nb_3Sn layers (i.e., the Nb_3Sn/Nb interfaces) and also regions close to the inner boundaries of the Nb_3Sn layers (towards the Sn-source core). Since in each filament the Nb_3Sn layer grows from the Sn-source core outwards into the unreacted Nb area, regions close to the inner boundary of the Nb_3Sn layer are formed first and are in the Nb_3Sn state for a longer portion of the reaction time than regions close to the outer boundary. It is clear from these images that for each of the three internal-oxidation wires (1.5Ti, 1Zr, 1Hf), the particles in the earlier-formed regions appear larger than those in the later-formed regions, suggesting that the particles may coarsen with heat treatment time. Here it is also worth mentioning that our study in [25] shows that the oxide particle size increases with reaction temperature.

It can be seen from Fig. 2 that the TiO_2 particles are much bigger than the ZrO_2 and HfO_2 particles. The TiO_2 particle size is about a few hundred nanometers in the earlier-formed Nb_3Sn region and ranges from ~10 nm to ~100 nm in the later-formed Nb_3Sn region in the 1.5Ti-675°C/250h. In contrast, the ZrO_2 particle size is mostly 5-10 nm (with a small percentage below 5 nm or reaching 15-20 nm) in the earlier-formed Nb_3Sn region, but drops to only a few nanometers (mostly below 5 nm, only a small percentage reaching 5-10 nm) in the later-formed Nb_3Sn region in the 1Zr-700°C/73h. The HfO_2 particles are even smaller than the ZrO_2 particles, with the majority of HfO_2 particles below 5 nm (and only a small percentage reaching 5-10 nm) in the earlier-formed Nb_3Sn region, and almost all HfO_2 particles in the 1-4 nm range in the later-formed Nb_3Sn region in the 1Hf-700°C/91h. In Fig. 2 it also appears that the particles at Nb_3Sn grain boundaries tend to grow bigger than those within Nb_3Sn grains.

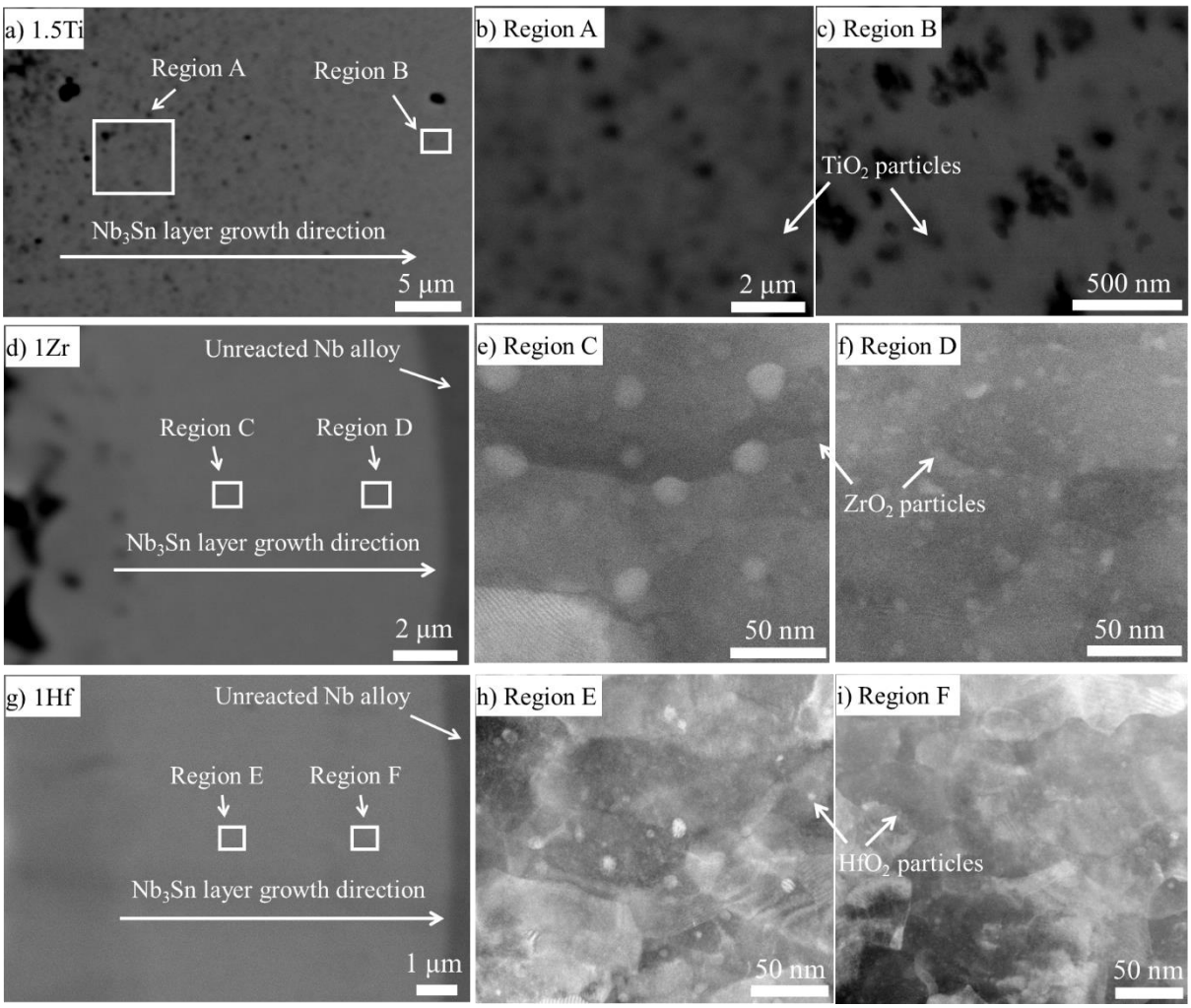

Fig. 2. (a) SEM image of a Nb_3Sn layer for 1.5Ti-675°C/250h, (b) SEM image for the Region A, (c) SEM image for the Region B, (d) SEM image of a Nb_3Sn layer for 1Zr-700°C/73h, (e) TEM image for the Region C, (f) TEM image for the Region D, (g) SEM image of a Nb_3Sn layer for 1Hf-700°C/91h, (h) TEM image for the Region E, (i) TEM image for the Region F.

3.2. Nb_3Sn grain size

Fig. 3 shows SEM images of fractured surfaces of all the six wires, all reacted at 675°C. We found that the grain size also varied as a function of position across the Nb_3Sn layer for all of the internally-oxidized wires (1.5Ti, 0.6Zr, 1Zr, and 1Hf). Fig. 3(a)-(f) show regions close to the outer boundaries of the Nb_3Sn layers, and Fig. 3(g)-(l) show regions close to the inner boundaries. For all of the internally-oxidized wires, it is seen that the earlier-formed Nb_3Sn grains are somewhat larger than the later-formed grains, similar to the particle size variation. Such a noticeable grain size increase from the newly-formed regions to the early-formed regions in a Nb_3Sn layer did not occur in the 4Ta or 1Hf-noO sample; in fact, it was not observed in the high-Sn-content versions of conventional, non-oxidation Nb_3Sn wires, either [20,21].

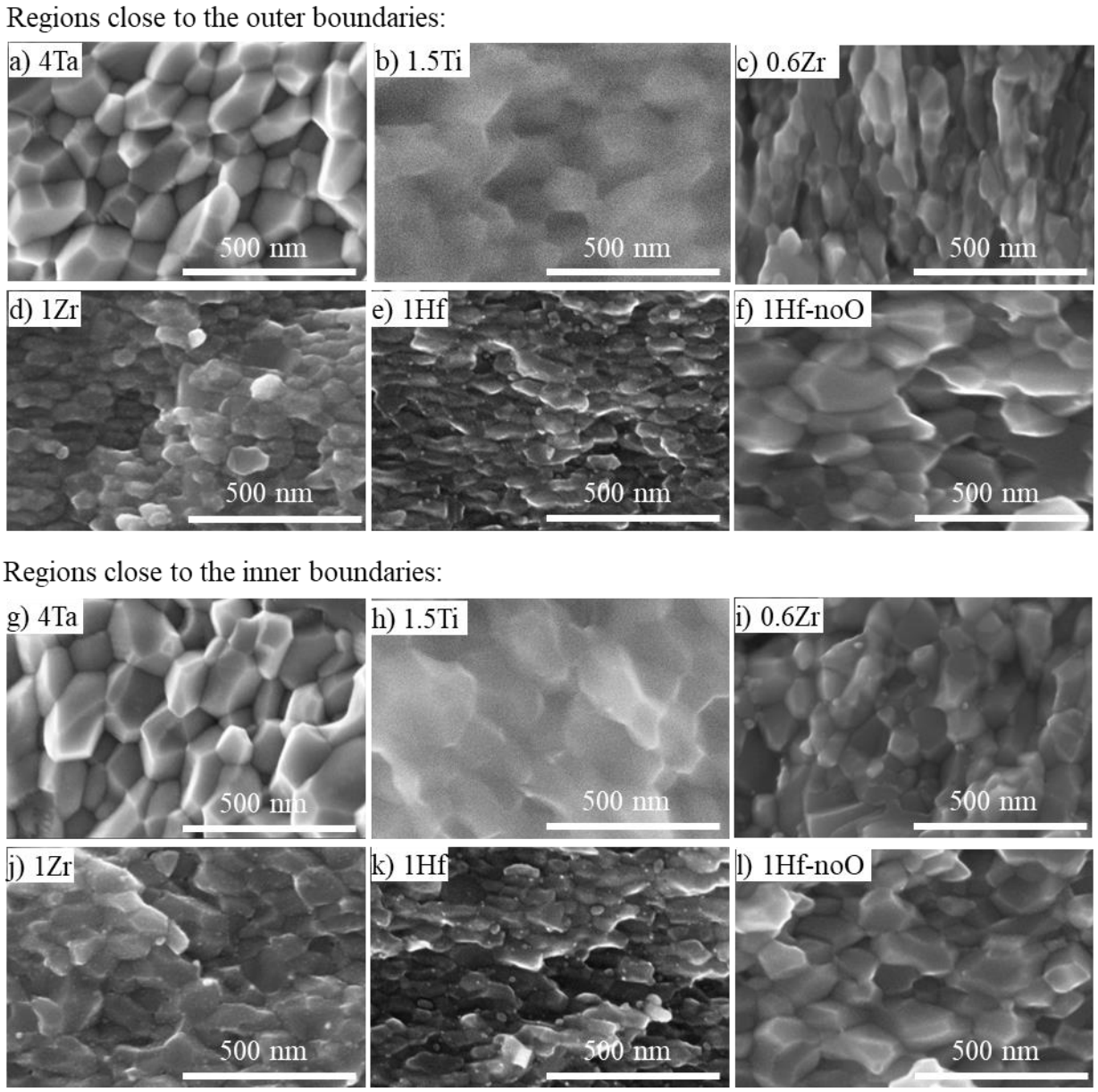

Fig. 3. SEM images of fractured surfaces of Nb_3Sn regions (a)-(f) close to the outer boundaries, and (g)-(l) close to the inner boundaries, for (a) and (g) 4Ta-675°C/90h, (b) and (h) 1.5Ti-675°C/250h, (c) and (i) 0.6Zr-675°C/152h, (d) and (j) 1Zr-675°C/250h, (e) and (k) 1Hf-675°C/280h, and (f) and (l) 1Hf-noO-675°C/70h, respectively.

The average grain sizes of these samples were calculated and are summarized in Table 2. The grain sizes of 4Ta or 1.5Ti were not noticeably smaller relative to conventional, non-oxidation Nb_3Sn [20,21]. This is not very surprising given the lack of particle formation in the 4Ta sample, and the relatively coarse precipitate array in the 1.5Ti sample. However, the refinement of grain

size was very obvious in the 0.6Zr sample, and was even stronger in the 1Zr, while the 1Hf sample had the most dramatic grain refinement among all the internal-oxidation samples. The grain sizes of the non-oxidation 1Hf-noO were somewhat smaller than those of 4Ta, demonstrating that Hf alloying without O can indeed refine Nb_3Sn grain size to a certain extent. However, the internally-oxidized 1Hf had significantly smaller grain size than the non-oxidation 1Hf-noO, indicating that internal oxidation, instead of the Hf alloying by itself, is most likely the primary cause of the grain refinement in our internally-oxidized Hf-alloyed wires. This is consistent with our previous results for Nb-Zr alloys, which showed that internal oxidation led to much smaller grain size compared with the non-oxidation control sample [5,15].

Table 2. Summary of the average grain sizes of the samples in Fig. 3 (all reacted at 675°C)

Sample	4Ta	1.5Ti	0.6Zr	1Zr	1Hf	1Hf-noO
Grain size close to the outer boundaries, nm	127	129	70	64	53	106
Grain size close to the inner boundaries, nm	130	141	87	81	62	98

3.3. F_p-B peak field shift

The measured F_p-B curves of all the samples are shown in Fig. 4, with each F_p-B curve normalized to its $F_{p,max}$ so that all curves can be clearly compared regarding peak field shift. The measured B_p values of all the samples are summarized in Table 3. In some previous work (e.g., [26,27]) B_{irr} values were obtained by fitting F_p-B curves using the equation: $F_P = \alpha(B/B_{irr})^{0.5}(1-B/B_{irr})^2 + \beta(B/B_{irr})(1-B/B_{irr})^2$, where α and β are fitting parameters. However, we decide not to use this method because the validity of this scaling relation has not been proven and Nb_3Sn inhomogeneity may cause a deviation from the ideal scaling relation [28]. Thus, here we use B_{irr} values directly extracted from the resistivity versus field (R-B) curves measured at high fields [17,18] (a criterion of 1% of the normal-state resistivity is used to determine B_{irr}), which are also given in Table 3 (only those Zr and Hf alloyed samples were measured). Detailed information about the R-B measurements can be found in [17,18].

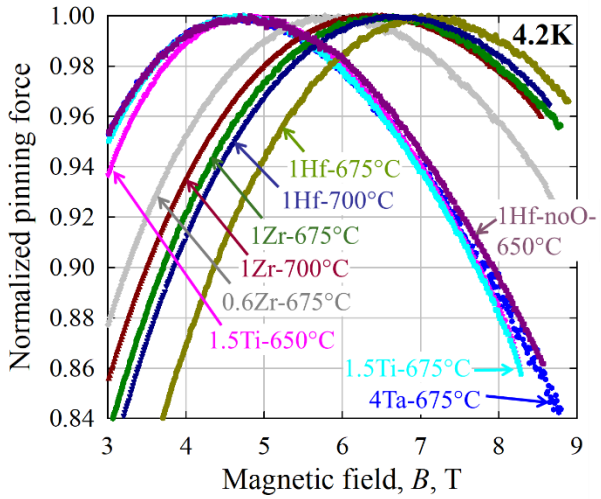

Fig. 4. Normalized magnetic F_p-B curves of all the samples.

Table 3. Summary of the B_p values, and some B_{irr} results from R-B measurements, along with the B_p/B_{irr} values

Sample	B_p, T	B_{irr}, T	B_p/B_{irr}
4Ta-675°C/90h	4.7	-	-
1.5Ti-675°C/250h	4.7	-	-
1.5Ti-650°C/350h	4.8	-	-
0.6Zr-675°C/152h	5.9	25.8	0.229
1Zr-675°C/250h	6.6	26.9	0.246
1Zr-700°C/73h	6.4	26.5	0.241
1Hf-675°C/280h	7.1	26.7	0.266
1Hf-700°C/91h	6.7	27.0	0.248
1Hf-noO-650°C/126h	4.9	25.4	0.193

Although the B_{irr} results of the 4Ta and 1.5Ti samples were not available, we found that the Kramer plots of their magnetic J_c-B curves had good linearity, indicating that they followed the conventional grain boundary pinning. This is perhaps due to lack of particles in the 4Ta sample and the too large TiO_2 particle size in the 1.5Ti samples. In contrast, internal oxidation of Nb-Zr led to much stronger F_p-B peak shift. The 1Zr wire reacted at 675°C had a B_p/B_{irr} of 0.246. Higher reaction temperature led to weaker F_p-B peak shift due to increase of particle size with reaction temperature [25], with the B_p/B_{irr} dropping to 0.241 for the 1Zr wire reacted at 700°C. Even reducing the Zr content to 0.63at.%, the shift was still considerable ($B_p/B_{irr} \approx 0.229$ for a reaction temperature of 675°C). Compared with Nb-Zr, internal oxidation of Nb-Hf led to even stronger shifts: the 1Hf wire reacted at 675°C had a B_p/B_{irr} of 0.266. Even raising the reaction temperature to 700°C, the 1Hf wire still had a B_p/B_{irr} of 0.248. On the other hand, the non-oxidation 1Hf-noO wire, even reacted at 650°C, had a linear Kramer plot and no F_p-B peak shift ($B_p/B_{irr} \approx 0.2$), which is consistent with our previous results for Nb-Zr alloys that there was no F_p-B peak shift if no O

was supplied [5,15]. This indicates that internal oxidation is needed for point pinning and F_p-B peak shift.

4. Discussion

First, let us explore what factors determine the grain size of internally-oxidized Nb_3Sn. This first requires a correct understanding of the mechanism for the grain refinement. We see from the comparison between the internally-oxidized 1Hf and the non-oxidation 1Hf-noO samples that although Hf alloying itself (without O) can moderately refine Nb_3Sn grain size, internal oxidation leads to a much stronger grain refinement. This, as well as the fact that for Zr alloying internal oxidation also leads to much smaller grain size than non-oxidation control [5,15], indicates that the grain refinement in internally-oxidized Nb_3Sn is primarily due to the generated oxide nanoprecipitates instead of the Hf (or Zr) alloying itself. The mechanism for the grain refinement by the precipitates is most likely the Zener drag effect – an important phenomenon in many material systems, in which dispersed particles exert a drag force on moving grain boundaries and thus cause grain size reduction by suppressing grain coarsening. For the Zener drag effect, a general relation is that $D \propto r/f$, where D is the grain size, r is the precipitate radius, and f is the volume fraction of the precipitates [29]. Thus, smaller particle size and higher particle volume fraction would lead to smaller grain size. In fact, this relation, combined with the oxide particle size variation (Fig. 2), explains the noticeable grain size variation across an internally-oxidized Nb_3Sn layer, which does not occur in high-Sn-content-version, non-oxidation Nb_3Sn. Provided that O content is sufficient, the precipitate volume fraction f is proportional to $x \cdot V_{m,oxide}/V_{m,A15}$, where x is the atomic fraction of the solute element in Nb (e.g., 1.5% for 1.5Ti), $V_{m,oxide}$ is the molar volume of the oxide, and $V_{m,A15}$ is the molar volume of Nb_3Sn (~44.6 cm^3/mol). The $V_{m,oxide}$ of ZrO_2 or HfO_2 can be calculated to be ~21.7 cm^3/mol, while that of TiO_2 is 21.1 or 18.9 cm^3/mol depending on its forms. Therefore, we obtain $D \propto r/x$ for each oxide. This relation can qualitatively explain the relative grain sizes of these samples, although a quantitative calculation is difficult because there may be other influencing factors as well. For example, although the 1.5Ti wire has a higher x value (1.5%) than that of 1Zr or 1Hf wire (1%), its much larger TiO_2 particle size leads to much weaker grain size reduction. In fact, the TiO_2 particles may be too large to cause an effective grain refinement. The 1Hf wire had smaller grain size than the 1Zr wire as a result of the smaller HfO_2 particle size. Higher solute content x leads to higher particle volume fraction and thus smaller grain size.

Next, let us consider the factors influencing the F_p-B peak field shift, which is determined by the ratio of point pinning force to grain boundary pinning force. It is interesting to see that smaller oxide particle size and higher volume fraction, on one hand leads to smaller Nb_3Sn grain size and thus higher grain boundary pinning, on the other hand also leads to higher point pinning due to higher volumetric density of particles, because the average number of particles per unit volume equals to $3f/(4\pi r^3)$. From the comparison of the B_p/B_{irr} values in Table 3, it is clear that with the decrease of particle size and increase of volume fraction, the increase of point pinning is faster than the increase of grain boundary pinning, causing a more dramatic F_p-B peak shift, which is

desirable. Given that increasing the precipitate volume fraction by increasing the solute content (assuming oxygen is sufficient) is limited by the drawability of the Nb alloy, reduction of oxide particle size is especially desirable. Next let us consider the factors influencing the precipitate size. To do this, it is needed to explore the nucleation and growth of the oxide precipitates.

(1) Nucleation. Based on classical nucleation theory, the driving force for the X and O solutes in the matrix to precipitate out is partly the reduction of Gibbs free energy when X and O react to form XO_2, and partly associated with a change in the strain energy in the matrix (e.g., elimination of the strain energy that is induced by the X and O solutes in the matrix); on the other hand, formation of XO_2 precipitates in the matrix would create new surfaces (interfaces between the precipitates and their surrounding matrix), which leads to increase of surface energy. For a spherical precipitate with radius r, the total Gibbs free energy change is $4\pi r^2\sigma - 4\pi r^3 \Delta G/3$, where σ is the surface energy per unit area and ΔG is the energy decrease for formation of unit-volume precipitation. Thus, the minimum precipitate radius r for the nucleation to occur is $r_{min} = 3\sigma/\Delta G$. The ΔG depends heavily on the energy reduction for the $X + 2O \rightarrow XO_2$ reaction: the higher affinity X has to oxygen, the larger this energy reduction is. For example, the standard formation energies for Nb_2O_5, Ta_2O_5, TiO_2, ZrO_2, and HfO_2 at 675°C are -594, -649, -770, -917, -930 kJ/mole-of-O_2, respectively. The formation energy of Ta_2O_5 is similar to that of Nb_2O_5, which is why Nb-Ta cannot be internally oxidized. It is possible that the low formation energy of TiO_2 partially accounts for formation of larger TiO_2 precipitate nuclei, but a thorough study of the strain energies for all of the solutes in the matrix and the surface energies for TiO_2, ZrO_2, and HfO_2 particles is needed to estimate their nucleation sizes. This will be explored in later work [25].

(2) Growth. The fact that the particle size is larger in the earlier-formed Nb_3Sn than that in the Nb_3Sn formed nearer the end of the reaction time suggests that the precipitates coarsen with heat treatment time. This indicates that Ti, Zr, Hf, and O atoms all must be able to diffuse within the Nb_3Sn. The growth of the particles depends on the diffusivities of these atoms: higher diffusivity leads to more particle coarsening. The diffusion rate may depend on several factors. First, these atoms may diffuse faster along Nb_3Sn grain boundaries than in the lattice – in fact, it indeed seems in Fig. 2 that the particles sitting at grain boundaries tend to be larger than those within Nb_3Sn grains. Second, they diffuse faster at higher temperature, which perhaps partially explains why higher reaction temperature leads to larger particle size [25]. Last but not least, the diffusivities of Ti, Zr, and Hf in Nb_3Sn may be different due to different atomic radius and mobility, etc., leading to different particle coarsening rate, which is worthy of further study.

In summary, from this work it can be seen that factors influencing grain size, oxide precipitate size and volume fraction, and F_p-B peak field shift in internally-oxidized Nb_3Sn include (in order of significance of the influence):

(1) Oxygen content. Oxygen content is found to be the most critical factor – it is seen from previous work [5,15] and this work that for both Zr alloying and Hf alloying, lack of oxygen leads to much weaker grain refinement as well as negligible point pinning or F_p-B peak field shift.

(2) Choice of solute element. From Ti to Zr and further to Hf, the ability to generate a dense set of fine oxide precipitates via internal oxidation increases, leading to dramatically smaller Nb_3Sn grain size and precipitate size as well as more pronounced F_p-B peak shift.

(3) Solute content. Assuming sufficient oxygen supply, higher solute content leads to increase in precipitate volume fraction, and thus stronger grain refinement and F_p-B peak shift.

(4) Reaction temperature. Lower reaction temperature leads to smaller precipitates in denser arrays, and thus stronger F_p-B peak shift.

Finally, it is worth briefly discussing the practical significance of F_p-B peak shift. It can be clearly seen from Fig. 4 that shift of F_p-B peak to higher fields strongly reduces J_c at low fields while enhancing J_c at high fields (even with the same $F_{p,max}$). While the J_c enhancement at high fields, where Nb_3Sn conductors are used, attracts extensive attention, the J_c reduction at low fields has been seldom paid attention to in the superconductor community, which is in fact also critical. This is because persistent-current magnetization, which is determined by the product of J_c and effective subelement diameter (d_{eff}), may cause several critical issues (e.g., flux jumps, field errors, hysteresis losses), and the magnetization of concern is primarily at low fields because low-field J_c is much higher than high-field J_c. Due to the high J_c required, the magnetization causes formidable field errors and a.c. losses in the FCC magnet design, which are imposing challenges to tackle [1,2]. A large reduction of d_{eff} while retaining high J_c is challenging for Nb_3Sn conductors; on the other hand, the significant reduction of low-field J_c in the APC Nb_3Sn offers a unique approach to combating the low-field magnetization problem [1].

5. Conclusions

This work explores the factors that influence the Nb_3Sn grain size, oxide precipitate size and volume fraction, and F_p-B peak field shift (which indicates point pinning contribution) for internal-oxidation-type Nb_3Sn superconductors. One influencing factor is the solute element of the Nb alloy used for internal oxidation. In this work we searched for all promising candidates and focused down on the group-IVB metals (Ti, Zr, Hf). We found that each of them can form oxide particles, but only those particles that are small in size and present with a high volume fraction can lead to dramatic effects, because smaller particle size and higher volume fraction lead to both higher grain boundary pinning (due to grain refinement) and higher point pinning (due to higher particle density), as well as stronger F_p-B peak shift. In this regard, we found that internal oxidation of Nb-Hf led to the strongest effects, Nb-Zr was a strong performer, while Nb-Ti showed negligible effects. Apart from the solute element, another critical factor is oxygen supply. It was found that for Hf alloying without oxygen, the point pinning was negligible and the grain size was much larger than Hf alloying + internal oxidation, indicating that the grain refinement in internally-oxidized Nb_3Sn is primarily due to the oxide particles (Zener drag effect) instead of Hf alloying itself. Other influencing factors include the solute content and heat treatment. Higher solute content leads to higher particle volume fraction, which leads to smaller grain size and more pronounced F_p-B peak shift. Lower reaction temperature leads to smaller precipitate size and thus more dramatic F_p-B peak shift. The mechanisms by which these factors influence the grain size and the

particle size were discussed, which may shed light on how to optimize these conductor design/processing factors in order to further improve Nb_3Sn superconductor performance. These results have an important implication for conductor development: since the needed high performance is at high fields, conductors that have a significant contribution of point pinning are most desirable. This suggests that internal oxidation is presently the best route to achieving the highest performance assuming conductor fabricability.

Declaration of interests

The authors declare that they have no known competing financial interests or personal relationships that could have appeared to influence the work reported in this paper.

CRediT authorship contribution statement

X. Xu: Methodology, Formal analysis, Investigation, Writing - original draft, Funding acquisition. **X. Peng:** Investigation, Funding acquisition. **J. Rochester:** Investigation. **M. Sumption:** Investigation, Writing - review & editing. **J. Lee:** Investigation. **G.A. Calderon Ortiz:** Investigation. **J. Hwang:** Investigation.

Acknowledgements

This work was supported by the LDRD program of Fermilab, the Early Career Research Program by US Department of Energy (DOE), as well as Hyper Tech SBIR DE-SC0013849 and DE-SC0017755 by US DOE.

References

[1]. A. Abada et al., FCC-hh: The Hadron Collider, Eur. Phys. J. Special Topics 228 (2019) 755–1107.
[2]. A. Ballarino, L. Bottura, Targets for R&D on Nb_3Sn conductor for high energy physics, IEEE Trans. Appl. Supercond. 25 (2015) 6000906.
[3]. D. Tommasini, F. Toral, Overview of magnet design options, CERN Report EuroCirCol-P1-WP5 (2016).
[4]. X. Xu, A review and prospects for Nb_3Sn superconductor development, Supercond. Sci. Technol. 30 (2017) 093001.
[5]. X. Xu, M.D. Sumption, X. Peng, Internally Oxidized Nb_3Sn Superconductor with Very Fine Grain Size and High Critical Current Density, Adv. Mater. 27 (2015) 1346-1350.
[6]. X. Xu, M.D. Sumption, X. Peng, Superconducting wires and methods of making thereof, U.S. Patent 9916919 (2018).

[7]. L. Motowidlo, P.J. Lee, C. Tarantini, S. Balachandran, A. Ghosh, D.C. Larbalestier, An intermetallic powder-in-tube approach to increased flux-pinning in Nb_3Sn by internal oxidation of Zr, Supercond. Sci. Technol. 31 (2017) 014002.
[8]. F. Buta et al., Superconducting properties and oxygen diffusion in Ta doped Nb_3Sn wires with internally oxidized ZrO_2, Applied Superconductivity Conference (2017) Wk2MOr3A-05.
[9]. M. Ortino, S. Pfeiffer, T. Baumgartner, X. Xu, M. Sumption, J. Bernardi, M. Eisterer, Evolution of the superconducting properties from binary to ternary APC-Nb_3Sn wires, submitted.
[10]. C. Buehler et al., Challenges and perspectives of the phase formation of internally oxidized PIT-type Nb_3Sn conductors, IEEE Trans. Appl. Supercond. 30 (2020) 6000805.
[11]. S. Balachandran, C. Tarantini, P.J. Lee, F. Kametani, Y. Su, B. Walker, W.L. Starch, D.C. Larbalestier, Beneficial influence of Hf and Zr additions to Nb4at.%Ta on the vortex pinning of Nb_3Sn with and without an O source, Supercond. Sci. Technol. 32 (2019) 044006.
[12]. T. Takeuchi, T. Asano, Y. Iijima, K. Tachikawa, Effects of the Iva Element Addition on the Composite-Processed Superconducting Nb_3Sn, Cryogenics 21 (1981) 585-590.
[13]. K. Tachikawa, H. Sekine, Method for producing superconducting Nb_3Sn wires, U.S. Patent 4323402 (1982).
[14]. M. Suenaga, D.O. Welch, R.L. Sabatini, O.F. Kammerer, S. Okuda, Superconducting Critical-Temperatures, Critical Magnetic-Fields, Lattice-Parameters, and Chemical-Compositions of Bulk Pure and Alloyed Nb_3Sn Produced by the Bronze Process, J. Appl. Phys. 59 (1986) 840-853.
[15]. X. Xu, M.D. Sumption, X. Peng, E.W. Collings, Refinement of Nb_3Sn grain size by the generation of ZrO_2 precipitates in Nb_3Sn wires, Appl. Phys. Lett. 104 (2014) 082602.
[16]. X. Xu, X. Peng, J. Lee, J. Rochester, M.D. Sumption, High Critical Current Density in Internally-oxidized Nb_3Sn Superconductors and its Origin, Scr. Mater. 186 (2020) 317-320.
[17]. X. Xu, M.D. Sumption, J. Lee, J. Rochester, X. Peng, Persistent compositions of non-stoichiometric compounds with low bulk diffusivity: a theory and application to Nb_3Sn superconductors, J. Alloys Compd. 845 (2020) 156182.
[18]. X. Xu, J. Rochester, X. Peng, M.D. Sumption, M. Tomsic, Ternary Nb_3Sn conductors with artificial pinning centers and high upper critical fields, Supercond. Sci. Technol. 32 (2019) 02LT01.
[19]. R.M. Scanlan, W.A. Fietz, E.F. Koch, Flux Pinning Centers in Superconducting Nb_3Sn, J. Appl. Phys. 46 (1975) 2244.
[20]. C.M. Fischer, Investigation of the relationships between superconducting properties and Nb_3Sn reaction conditions in powder-in-tube Nb_3Sn, M.S. Thesis, University of Wisconsin-Madison 2002.
[21]. X. Xu, M.D. Sumption, E.W. Collings, Influence of Heat Treatment Temperature and Ti doping on Low Field Flux Jumping and Stability in $(Nb\text{-}Ta)_3Sn$ Strands, Supercond. Sci. Technol. 27 (2014) 095009.
[22]. E.J. Kramer, Scaling Laws for Flux Pinning in Hard Superconductors, J. Appl. Phys. 44 (1973) 1360-1370.
[23]. D. Dew-Hughes, Flux pinning mechanisms in type II superconductors, Phil. Mag. 30 (1974) 293-305.
[24]. S. Hong, Unpublished data.

[25]. J. Lee, Z. Mao, D. Seidman, X. Xu, Unveiling the nucleation and growth of Zr oxide particles of internally-oxidized Nb_3Sn superconductors, to be submitted.
[26]. D. Rodrigues, L.B.S. Da Silva, C.A. Rodrigues, N.F. Oliveira, C. Bormio-Nunes, Optimization of Heat Treatment Profiles Applied to Nanometric-Scale Nb_3Sn Wires With Cu-Sn Artificial Pinning Centers, IEEE Trans. Appl. Supercon. 21 (2011) 3150-3153.
[27]. T. Baumgartner, M. Eisterer, H.W. Weber, R. Flükiger, C. Scheuerlein, L. Bottura, Performance Boost in Industrial Multifilamentary Nb_3Sn Wires due to Radiation Induced Pinning Centers, Sci. Rep. 5 (2015) 10236.
[28]. T. Baumgartner, S. Pfeiffer, J. Bernardi, A. Ballarino, M. Eisterer, Effects of inhomogeneities on pinning force scaling in Nb_3Sn wires, Supercond. Sci. Technol. 31 (2018) 084002.
[29]. N. Ryum, O. Hunderi, E. Nes, On Grain Boundary Drag from Second-Phase Particles, Scr. Metall. 17 (1983) 1281–1283.